Hierarchical synchrotron diffraction and imaging study of the calcium sulfate hemihydrate–gypsum transformation

Michela La Bella, Rogier Besselink, Jonathan Wright, Alexander van Driessche, Alejandro Fernandez-Martinez, Carlotta Giacobbe

Hierarchical synchrotron diffraction and imaging study of the calcium sulfate hemihydrate-gypsum transformation

Authors

Michela La Bella[ab]*, Rogier Besselink[b], Jonathan P. Wright[a], Alexander E. S. Van Driessche[bc], Alejandro Fernandez-Martinez[b] and Carlotta Giacobbe[a]

[a] European Synchrotron Radiation Facility, 71 Avenue Des Martyrs, Grenoble, 38040, France

[b] Univ. Grenoble Alpes, Univ. Savoie Mont Blanc, CNRS, IRD, IFSTTAR, ISTerre, 38000 Grenoble, France

[c] Instituto Andaluz de Ciencias de la Tierra (IACT), CSIC-University of Granada, 18100 Armilla, Granada, Spain

Correspondence email: michela.la-bella@esrf.fr

Abstract The mechanism of hydration of calcium sulfate hemihydrate ($CaSO_4 \cdot 0.5H_2O$) to form gypsum ($CaSO_4 \cdot 2H_2O$) was studied by combining scanning 3D X-ray diffraction (s3DXRD) and phase contrast tomography (PCT) to determine *in-situ* the spatial and crystallographic relationship between these two phases. From scanning 3DXRD measurements, we obtained the crystallographic structure, orientation, and position of the crystalline grains in the sample during the hydration reaction, while the PCT reconstructions allowed us to visualize the 3D shapes of the crystals during the reaction. This multi-scale study unfolds structural and morphological evidence of the dissolution-precipitation process of the gypsum plaster system bringing insights on the reactivity of specific crystallographic facets of hemihydrate. In this work, epitaxial growth of gypsum crystals on the hemihydrate grains was not observed.

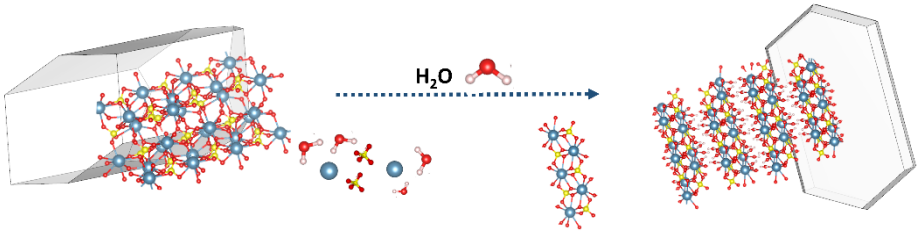

Keywords: Scanning 3DXRD, diffraction, PCT, gypsum, hemihydrate.

1. Introduction

Gypsum plaster, or stucco, or "plaster of Paris" is the material made by the hydration of calcium sulfate hemihydrate ($CaSO_4 \cdot 0.5H_2O$) resulting in the formation of calcium sulfate dihydrate or gypsum ($CaSO_4 \cdot 2H_2O$). Gypsum plaster has been used as a construction material since the Neolithic period (de Brito & Flores-Colen, 2015), and it is an important material for construction due to its low cost and to the high availability of the raw materials. The global consumption of both crude and calcined gypsum from the first to the third quarter of 2022 has been estimated around 44,500,000 metric tons (US Geological Survey, Mineral Industry Surveys, Gypsum in the third quarter of 2022). The cohesive properties due to the needle-like morphology of the crystals, make gypsum plaster a useful material for structural applications, as well as internal coatings (Pedreño-Rojas *et al.*, 2019) (de Brito & Flores-Colen, 2015) and as an additive for the setting of cement (Taylor Harry FW, 1997). The biocompatibility of gypsum makes it suitable for medical applications i.e. dentistry and orthopaedics (Thomas & Puleo, 2009) and as an excipient in the pharmaceutical industry (Carretero & Pozo, 2009).

Calcium sulfate is present in nature in three different minerals: anhydrite ($CaSO_4$), calcium sulfate hemihydrate or bassanite ($CaSO_4 \cdot 0.5H_2O$) and gypsum ($CaSO_4 \cdot 2H_2O$). The common structural characteristic for all these phases is the presence of chains of sulfate tetrahedra and calcium ions. In the case of gypsum, a layered structure is present with a hydrated interlayer that results in a preferential cleavage plane along the [010] direction. In the hemihydrate structure, the water molecules are placed into water channels parallel to the [001] direction (Freyer & Voigt, 2003). A projection of the crystal structure of hemihydrate (a) and gypsum (b) is shown in Figure 1.

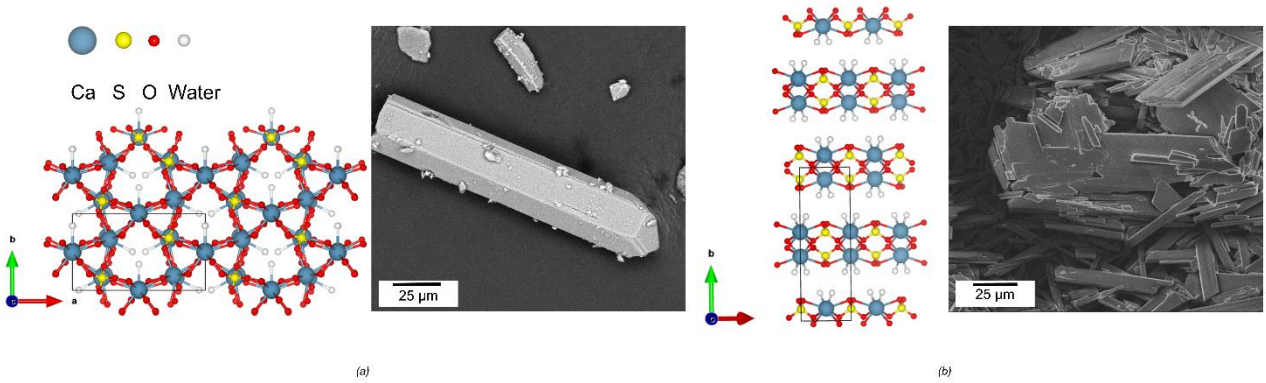

Figure 1 (a) Crystallographic structure of the calcium sulfate hemihydrate (Ballirano *et al.*, 2001) along the *c* direction and SEM image of typical α-hemihydrate crystal. (b) Crystallographic structure of calcium sulfate dihydrate (Boeyens & Ichharam, 2002) along the *c* direction and SEM image of an aggregate of gypsum crystals showing different sizes and shapes. The SEM pictures have been taken with a VEGA3 TESCAN scanning electron microscope with a voltage of 16 kV. Legend: blue balls = Ca atoms; yellow balls = S atoms; red balls = O atoms; white balls = water molecules.

To obtain gypsum plaster, the hemihydrate is hydrated with aqueous solutions leading to the formation of gypsum plaster via the following exothermic reaction (Eq. 1):

$$CaSO_4 \cdot 0.5\ H_2O + 1.5\ H_2O \rightarrow CaSO_4 \cdot 2H_2O + Q \quad (1)$$

Where Q is the heat generated by the exothermic reaction. As for most cementitious materials, also for gypsum plaster, the development of its strength is strongly related to its setting process (Lewry & Williamson, 1994). The dissolution of the hemihydrate continues to drive concentration gradients in the supersaturated solution while gypsum crystals are growing. The nucleation and growth rates of gypsum crystals has previously been followed by in-situ X-ray tomography (Adrien *et al.*, 2016). The kinetics of these processes are controlled by thermodynamic drivers (saturation state of the interfacial water layers in the pores between the hemihydrate crystals) and by kinetic barriers associated with the dissolution and precipitation pathways. Micro-textural properties also affect the hydrodynamics and mixing of the aqueous solutions (Singh & Middendorf, 2007). Precise crystallographic studies of hemihydrate to gypsum transformation, to determine which are the most reactive crystallographic facets during both hemihydrate dissolution and gypsum growth, should help to control the plaster hydration reaction.

Hydration rates are known to alter the final porous microstructures of entangled gypsum crystals (Singh & Middendorf, 2007), but the models describing the crystallization of gypsum are still debated. Despite extensive study, it has been only in recent years, and due to non-destructive methods based on synchrotron X-ray radiation, that a non-classical nucleation model has been proposed to explain the early stages of gypsum crystallization (Van Driessche *et al.*, 2016). This complex process involves (i) the formation of a precursor phase, (ii) its aggregation and (iii) coalescence/reorganization forming gypsum crystals (Wang *et al.*, 2012) (Van Driessche *et al.*, 2012) (Saha *et al.*, 2012). A detailed examination of each of these steps (Stawski *et al.*, 2016) and the structural characteristics of the precursor units (Stawski *et al.*, 2019) results in a complete view of the crystallization process.

Crystal nucleation and growth both determine the development of the microstructure of the final gypsum material. Due to the critical role that the evolution of the microstructure plays for the development of the properties of gypsum plaster, providing *in-situ* observations of how the microstructure forms and sets is essential. Recently, studies using X-ray tomography (both with lab equipment and synchrotron sources) have provided insights on the kinetics of dissolution and growth of hemihydrate and gypsum crystals, and on the porosity of the material. The first *in-situ* X-ray tomography study is attributable to Adrien et al. 2016 (Adrien *et al.*, 2016). This study was carried out with a laboratory tomography equipment and allowed to follow qualitatively and quantitatively the kinetics of the reaction. Recently, another *in-situ* study probed the hydration reaction of α-hemihydrate using synchrotron X-ray tomography with unprecedented time (30-40 s) and space (0.163 μm voxel size) resolution (Seiller *et al.*, 2021). These works provide a clear view of the

morphologies of the grains involved in the reactions. However, crystallographic information are also needed to establish precise structure-reactivity-microstructure relationships.

In previous works (Artioli *et al.*, 2015) (Artioli *et al.*, 2010) (Claret *et al.*, 2018) focused on detecting calcium silicate hydrate (C-S-H), ettringite and carbonation during the hydration of cements, X-ray diffraction computed tomography (XRD-CT) was applied. In these cases, the diffraction spots were filtered out from the data in order to simplify the diffraction tomographic reconstruction problem and to focus on the role of the amorphous phases. In this paper, in order to follow the growth kinetics of larger crystals, it is instead essential to include these diffraction spots in the reconstructions. The s3DXRD is a recently developed synchrotron-based technique that can be used to locate and separate individual crystals in polycrystalline or grained (powdered) samples, and determine their size, shape and crystallographic orientation in three dimensions based on the X-ray diffraction patterns. The s3DXRD technique was originally developed for metallurgical research due to the high potential that multigrain crystallography offers for studying the evolution of polycrystalline materials (Hayashi *et al.*, 2015) (Hayashi *et al.*, 2014) (Poulsen, 2004). The scanning method allows us to reconstruct structural features that are smaller than the size of the individual crystals. Differences between the surface and the bulk of the crystal can be resolved, as well as any other strain or orientation gradients. Grain or twin boundary locations and shapes within growing agglomerates can also be extracted from the s3DXRD reconstructions, while these are not detectable in tomography. The scanning method was previously applied on tin whisker growth (Hektor *et al.*, 2019) (Henningsson *et al.*, 2020) with submicron spatial resolution where the initial and final states of phases and strains could be mapped in the same sample before and after annealing. Another recent application of s3DXRD is the work of Hayashi et al. 2019 (Hayashi *et al.*, 2019). They reconstructed intragranular stress tensors on bulk steel, providing a way to predict possible deformations of the material. The s3DXRD applications show the potential of s3DXRD to probe crystallographic and microstructural properties such as crystallite size and strain at the sub-micron scale, making it a perfect probe to determine the reactivity of polycrystalline and fine-grained materials.

Here, we used a combination of PCT and s3DXRD to follow *in-situ* the setting process of plaster. PCT gives the morphological and spatial evolution of all the components of the hydration reaction. Crystallographic information such as phase, lattice and orientations of all the crystalline components of the system can be found by s3DXRD. The complementarity of these different methods gave multi-modal and multi-scale snapshots of the hydration reaction of gypsum plaster that give detailed insights of the dissolution and precipitation reactions taking place.

2. Experimental

2.1. Materials and pre-characterization

A sample of α-hemihydrate was precipitated by mixing two equimolar solutions of Na_2SO_4 (Roth®, > 99 %) and $CaCl_2$ (Roth®, > 99 %) in a 5 M solution of NaCl (Ossorio *et al.*, 2014). The solution was kept in the oven at 90 °C for ~1 h after mixing, and was subsequently filtered with a vacuum-filtering system. The obtained slurry was washed several times with ethanol to minimize the presence of NaCl crystals. The sample was subsequently pre-characterized with Scanning Electron Microscopy (SEM) and Fourier-Transform Infrared spectroscopy (FTIR). SEM images provided qualitative observations about the shape and size of the hemihydrate crystals. A LEO 1530 (Gemini) scanning electron microscope at a voltage of 10 kV and 9 mm working distance was used. A small amount of sample was deposited onto a carbon tape mounted on an Al stub and gold-coated (50 nm). Images were then collected using the signal of both back-scattered and secondary electrons. Mid-infrared FTIR spectra were collected to verify the purity of the samples. A Nicolet IS50R Research FTIR Spectrometer using the Attenuated Total Reflectance sample holder with a single-reflexion diamond crystal was used. Once the purity and the size of the crystals were verified, a quartz capillary with a 0.3 mm internal diameter was filled with the crystals. The hydration of the hemihydrate crystals was then started by adding a saturated aqueous calcium sulfate solution to the capillary with a syringe in order to follow the hydration reaction of the sample *in-situ*.

2.2. Powder diffraction

In order to check the unit cell of α-hemihydrate for the s3DXRD indexing process, a high-resolution powder diffraction pattern was collected at ID22, the High Resolution Powder Diffraction beamline of the European Synchrotron Radiation Facility (ESRF), using a monochromatic X-ray beam at an incidence energy of E = 35 keV (λ = 0.35389 Å) . Data was recorded at room temperature in the −5 to 30° 2θ range using the combination of multi-analyzer crystals and a 2D HPC-detector (Dectris Eiger2 X CdTe 2M-W), and merged together using the *in-house* software id22sum (Dejoie *et al.*, 2018). Le Bail fits implemented in TOPAS5 (Coelho, 2018) were then performed to confirm the unit cell of the hemihydrate. Powder diffraction patterns, were as well collected at ID11, the Materials Science beamline of the ESRF. Two data collections were performed, one of the starting dry hemihydrate and one after the hydration process, to assess whether the hydration reaction had fully or partially taken place. The experimental setup was the same used for the s3DXRD (Figure 2) with the exception that a beam size of 250 × 250 µm instead of 5 × 5 µm was used in order to give a better powder average. The patterns were collected in the 1-10° 2θ range at an energy of 43.575 keV (λ = 0.2843 Å). Preliminary instrumental calibration at ID11 was performed using a CeO_2 powder standard using the *pyFAI-calib* tool and integrated with *pyFAI-integrate* (Ashiotis *et al.* 2015).

2.3. S3DXRD

In-situ s3DXRD experiments were conducted at the 3DXRD station of ID11 (Poulsen, 2004). The analysed specimen contained calcium sulfate hemihydrate grains in a glass capillary with a diameter

of 0.3 mm. The first data collection was performed with the sample in dry conditions, and a second dataset was taken 36 h after starting the hydration process in the capillary. A monochromatic beam at an energy of 43.575 keV (Nd edge) was focused to a size of 5×5 μm using aluminium compound refractive lenses. A pencil beam approach was used, having the beam size significantly smaller than the average size of the grains. The sample was scanned horizontally along the *y* direction (across the beam direction) with a Δ*y* step equal to the beam width of 5 μm. The datasets were collected with an angular step of Δω=1° over rotations between 0° and 180°, and exposure time of 0.08 s. The detector used was a FreLoN2k camera, with 2048 × 2048 pixels of 47.2 × 47.2 μm, placed at 154 mm from the sample. The capillary was mounted with its longitudinal direction parallel to the *z* direction as represented in the scheme in Figure 2a. The diffraction spots coming from the rotation of the grains were collected as 2D images from the detector. A schematic representation of the s3DXRD data acquisition is shown in Figure 2a.

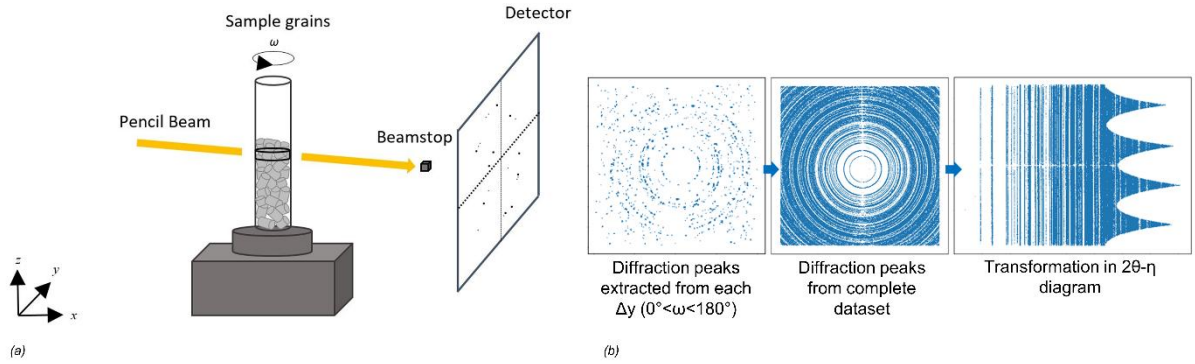

Figure 2 (a) Schematic representation of the experimental setup of the 3DXRD microscope at ID11 (ESRF, France). A glass capillary filled with calcium sulfate hemihydrate grains, was mounted on the rotation stage and translated in the *y* direction. During the rotation, the diffraction spots coming from the grains were collected onto the detector. A beamstop was placed in front of the center of the detector in order to absorb the direct beam and prevent damaging the detector. (b) Segmentation method workflow with the *ImageD11* software: from the extraction of the diffraction peaks from one rotation (0° < ω < 180° at one Δ*y*), to the extraction of the peaks of the full dataset and finally the azimuthal integration of the diffraction pseudo-rings and representation of the peaks in the 2θ-η diagram.

The s3DXRD data analysis consists of the indexing and refinement of the grains. The indexing and refinement of the polycrystalline diffraction spots were done with Jupyter notebooks based on the *ImageD11* software that is part of the FABLE complete suite for 3DXRD data treatment (Wright 2005) (Sørensen *et al.*, 2012) (Hayashi *et al.*, 2015). *ImageD11* permits to segment the diffraction spots from the detector images and to determine their center of mass positions. The scattering vectors are calculated from the calibrated instrument geometry. A schematic representation of the

segmentation sequence used for the two datasets is shown in Figure 2b. After locating spots for all the images, these were transformed into a 2θ-η diagram to identify the crystallographic phases and check for possible texture. For the hemihydrate sample (initial state), the majority of the grains could be indexed using the known unit cell. For the hydrated sample, only the largest gypsum crystals were indexed. This selection was done using a higher threshold of intensity for the segmentation step that allowed also to avoid problems with spot overlaps. By segmenting and indexing only the diffraction spots coming from the larger crystals of gypsum, the smaller grains were discarded. For the indexing process of both datasets, only selected rings for the appropriate phases were used to generate trial orientation matrices (UBI matrices that are the inverse of the conventional (UB) (Busing & Levy, 1967)). Grains were only retained if they indexed a certain number of peaks (1000 for hemihydrate grains and 500 for gypsum grains). Then the orientation matrices and the center of mass of the indexed grains were refined and the position and shape of the crystals in the space were reconstructed within a grain map (Hektor *et al.*, 2019). The iradon transformation of the sinograms, made by the indexed peaks, of each grain gave the position and shape of the grains in the grain map.

2.4. PCT

In-situ PCT measurements were performed during the same experiment at ID11. The energy was not changed from the s3DXRD measurements but the setup presented few differences. Here, no focusing optics were used and the projections were recorded with an imaging detector (FreLoN4M camera with region of interest (ROI) of 500 × 550 pixels) placed at 300 mm downstream from the sample to enhance the phase contrast. The relatively large distance was chosen in order to give good phase contrast between the different components of the sample while retaining good spatial resolution. A 10x magnification lens was used, providing a voxel size of 1.56 μm. Since PCT and s3DXRD data collections where acquired sequentially by changing the beam width and detector, the measurements were performed on the same sample. A first measurement was performed before the hydration of the sample in order to characterize the dry hemihydrate grains. Following measurements were taken every 30 minutes after the injection of the solution in the capillary. The last measurement was acquired after 36 hours of hydration to match the final s3DXRD data.

The projections of the sample were collected over rotations in $\omega = 0° < \omega < 360°$ with a total of 500 images per rotation. The datasets were reconstructed using ESRF inhouse software. *Tomwer* and *Nabu* were used to apply the dark and flat field corrections and subsequently reconstruct transversal slices of the sample with the filtered back projection algorithm (Shepp & Logan, 1974). In order to segment grains from the surrounding solution and air bubbles, the Paganin phase retrieval algorithm (Paganin *et al.*, 2004) was applied during the reconstruction. The most suitable delta/beta value was $\delta/\beta = 30$, giving the best compromise between sharpness and contrast to segment phases in the images. The reconstructions were segmented to locate grains of hemihydrate and gypsum and to

follow the evolution of the microstructure of the plaster during the hydration. A few selected grains of both hemihydrate and gypsum, which were also indexed in the s3DXRD data, were segmented manually (with the ROI painter tool of the *Dragonfly* software). In this case, to allow a clearer enhancement of the edges of the grains, no Paganin filter was applied. Preliminary visualization of the images was performed using both *ImageJ/Fiji* (Abramoff M. D. *et al.*, 2004) and *Dragonfly* (version 2021.1, Object Research System (ORS) Inc., Montreal, Canada). The 3D rendering of the volumes of the full sample and the single grains together with the calculation of volumes and surface area of dissolving hemihydrate and growing gypsum crystals were done with *Dragonfly*.

3. Results

3.1. Pre-characterization results

SEM images of the hemihydrate crystals used as starting material for the hydration show the typical shape and size associated with the α-hemihydrate phase (Singh & Middendorf, 2007). Crystal sizes shown in Figure 3a are between 60 and 100 μm. Except for some small fragments, they all display an elongated and pencil-shaped crystal habit. In Fig. 3b, one single grain of hemihydrate is shown. As expected for the α-hemihydrate, it is characterized by an euhedral habit with well-defined edges separating the different crystallographic faces. It is possible to recognise three characteristic crystallographic planes: in yellow the {111} facets, in red the {100} facets, and in green the {011} facets.

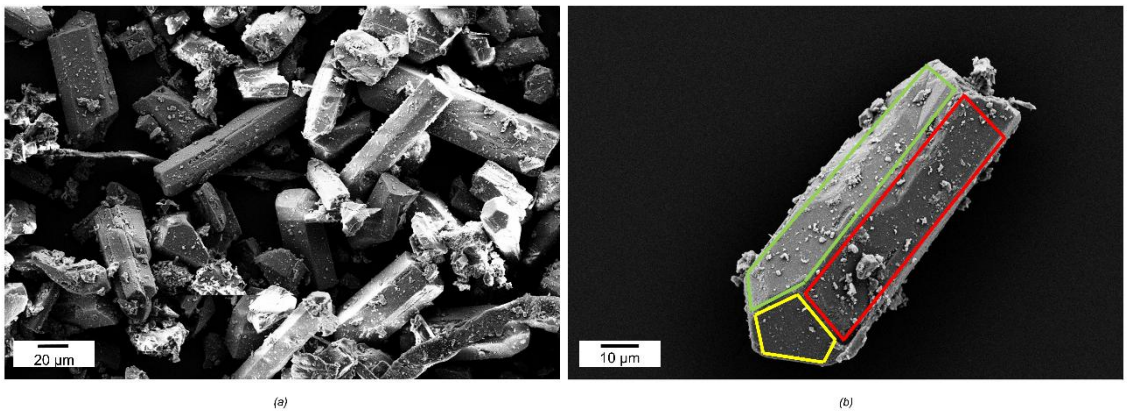

Figure 3 SEM pictures of the starting material synthesized and used for the realization of this work. (a) An agglomerate of α-hemihydrate crystals. (b) Detail of a single hemihydrate crystal, showing the typical crystal habit and pencil-shape tip of the α-hemihydrate. Some crystallographic planes are recognisable: {111} facets in yellow, {100} facets in red, {011} facets in green.

The starting material was also characterized using FTIR. The absorbance spectrum (shown in S1) shows absorption bands in the regions of scissoring of water (around 1596 cm^{-1}), OH-stretching of water (3652 and 3756 cm^{-1}) and in the region associated with the vibration of SO_4^{2-} ions (around

1000-1200 cm^{-1}). The spectrum is in agreement with previously reported calcium sulfate hemihydrate spectra (both α and β), and showed no contribution from gypsum (Bensted & Varma, 1971) (Pons-Jiménez *et al.*, 2015).

3.2. PCT results

From the reconstruction of the transversal slices of the capillary, it is possible to navigate inside the sample and select a region of interest to follow the evolution of a specific set of particles. In Figure 4a-p a collection of slices of the capillary are shown corresponding to the same layer of the sample scanned using s3DXRD. Each slice corresponds to a different time of hydration. From the first slice (dry hemihydrate) to the last one (36 hours of hydration) it is possible to observe the progressive dissolution of hemihydrate crystals and the formation of a network of smaller and interlocked gypsum crystals. The last slice (Figure 4p) corresponds to the presence of mostly gypsum inside the capillary. Images q-t of Figure 4 show in detail the dissolution of two hemihydrate grains, which were monitored until full dissolution. In Figure 4q and 4r the two hemihydrate grains are clearly recognisable, in Figure 4s they are almost completely dissolved and in Figure 4t the hemihydrate grains are replaced with a dense gypsum network. The choice of these two specific grains has been made because of their different orientations in the capillary. The first grain from the left is viewed parallel to its longitudinal axis, showing the pseudo-hexagonal shape of the crystal. The second particle displays the typical elongation of the α-hemihydrate crystals. In Figure 4a the hemihydrate crystals show their original shape. In Figure 4c, after 1 h of hydration, the formation of small crystals of gypsum starts to be visible around the bigger hemihydrate grains. Moving to Figure 4o, corresponding to 20 hours of hydration, the two hemihydrate grains are almost completely dissolved while the network of gypsum crystals further grows around the hemihydrate fragments. Figure 4p, corresponding to the last measurement after 36 h of hydration, shows the replacement of the hemihydrate by a complex matrix made of needles and plate shaped gypsum crystals interlocked with each other.

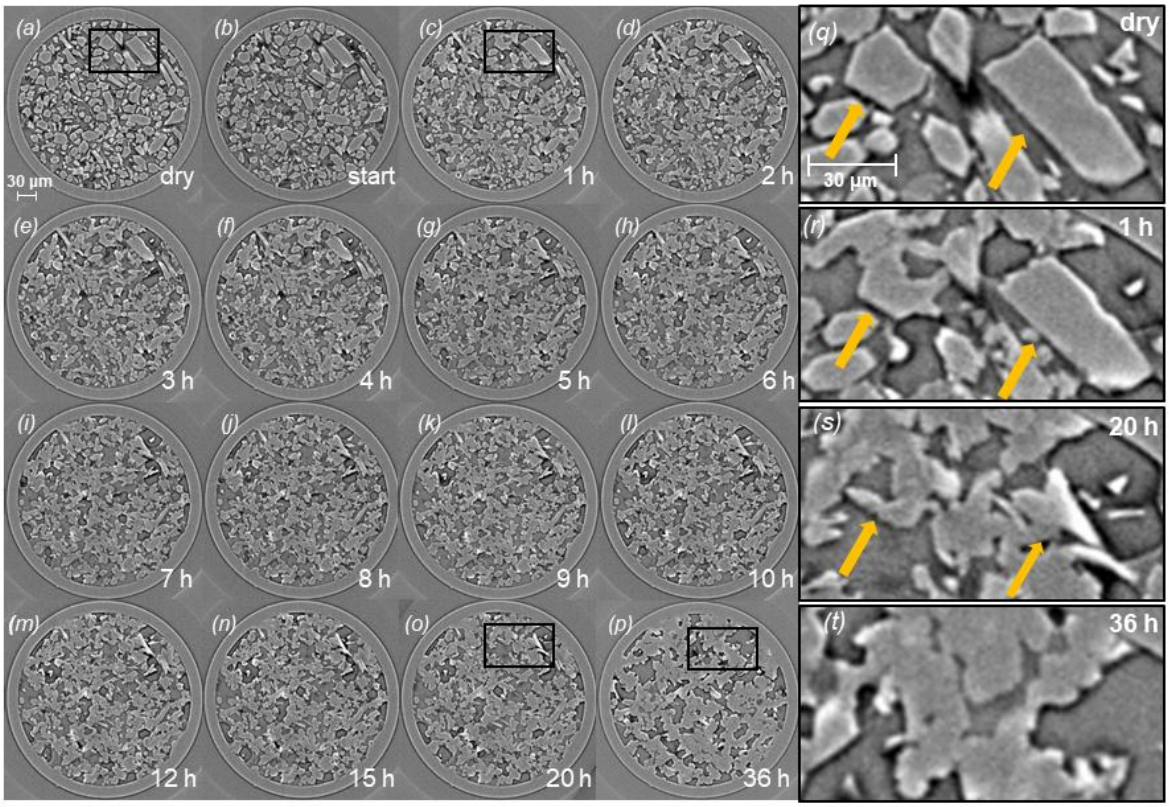

Figure 4 **(**a-p) Collection of slices at different hydration stages. The first slice corresponds to the sample in its dry starting condition. From the second slice to the last one 36 hours of hydration have passed. As the hydration process takes place the initial hemihydrate grains are progressively dissolved and small crystals of gypsum are forming and growing in an intricate network. (q-t) Zoom of a particular area of the sample, highlighted in (a-c-o-p), followed over the hydration reaction in order to show in detail the dynamic of dissolution of two selected hemihydrate grains and the formation of gypsum crystals around them until the complete replacement of α-hemihydrate by gypsum.

In order to visualize better their dissolution in 3D, the two hemihydrate particles followed in Figure 4 q-s were segmented and extracted from the whole volume. Figure 5 shows the evolution of the 3D volumes of both hemihydrate grains throughout the hydration process, starting from the dry conditions (5a), to 2 h of hydration (5b), then to 8 h (5c) and finally to 12 h (5d). The reconstruction of the dissolution of the grains confirms what is already visible from the 2D slices in Figure 4 q-t. The two crystals are slowly dissolving showing the formation of a layered texture at the surfaces that seems to suggest a preferential dissolution of the grains along the elongated axis. The two crystals maintain an elongated shape even when they are close to complete dissolution (Figure 5d).

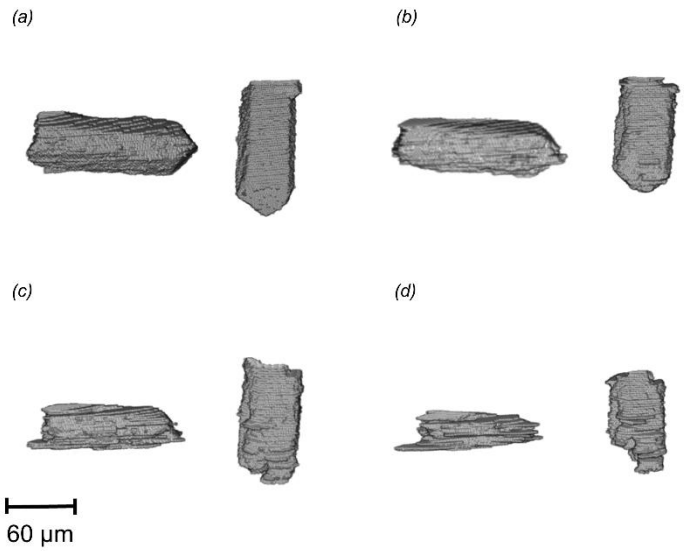

Figure 5 3D reconstruction of the two α-hemihydrate crystals with different orientations. The volume of the two grains was reconstructed in order to visualize the textural features of the dissolution process. (a) dry conditions. (b) 2 h of hydration. (c) 8 h of hydration. (d) 12 h of hydration.

After the reconstruction of the 3D volumes of each dataset, they were segmented in order to discriminate between the different constituents of the sample. Figure 6 shows a series of 3D reconstructions of half of the volume of the capillary over time. The volumes have been cut in half to show how the micro-texture evolves from the presence of only large hemihydrate crystals to the growth of gypsum. An evolution of the grain morphologies over time can be observed. The intermediate stages show how gypsum initially nucleates and grows in the pore spaces between the hemihydrate grains. The gypsum network starts to form with small agglomerates of needle shaped crystals and ends with the presence of larger plate-shaped crystals.

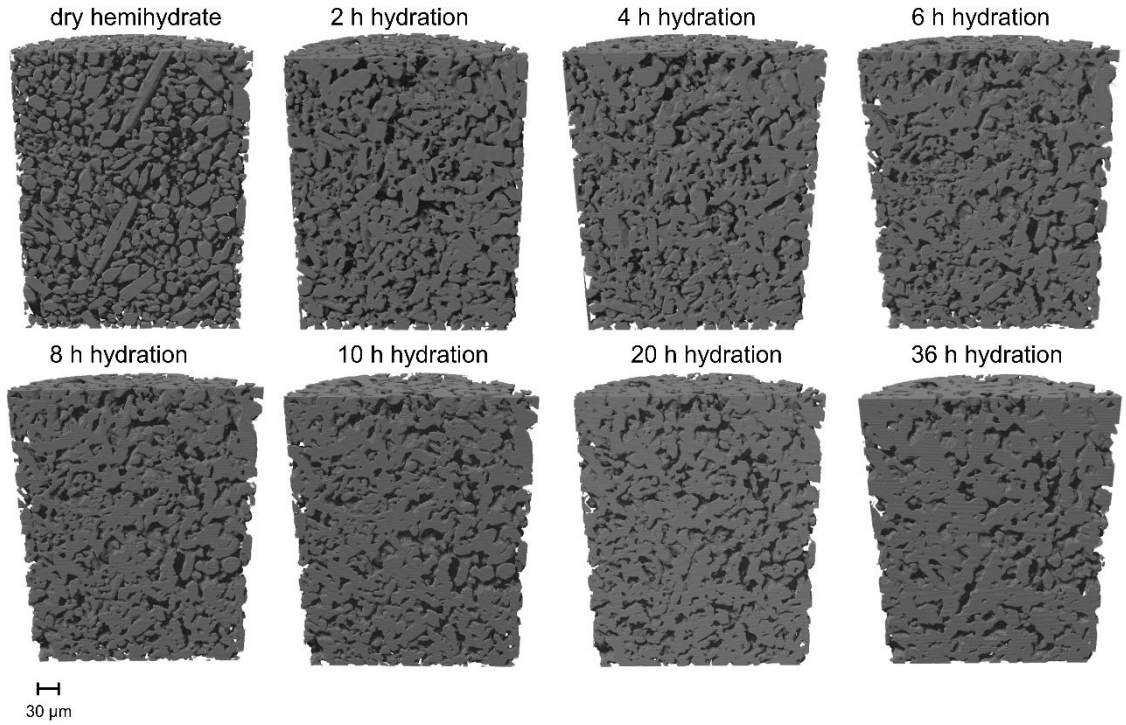

Figure 6 PCT 3D reconstructions of the volume of the sample during the hydration process. The volumes show the inside of the capillary during the development of the hydration process of hemihydrate. The reconstructions start with a capillary filled with dry hemihydrate grains and ends with the sample containing gypsum crystals.

3.3. S3DXRD results

3.3.1. Grain maps

Following the segmentation of the detector images of the dry hemihydrate dataset, and the extraction of the diffraction spots, we indexed 107 hemihydrate grains using the monoclinic cell I2 refined by Ballirano et al. 2001 (Ballirano *et al.*, 2001). The indexing process works better for larger crystals because they produce stronger diffraction spots that are easier to locate, providing also more pixels for crystal shape reconstruction. For this study, only the crystals that were large enough to offer meaningful shape information were added to the grain map for correlation with the PCT data. While building the sinogram of each indexed grain, all of the peaks which are close to ideal scattering vectors are potentially assigned via the indexing process. Once the iradon transformation was performed on the sinogram for each indexed grain, the reconstructions were treated to remove the background noise (i.e. peaks that are not coming from this grain). To do so, a threshold was applied to the intensity values of each pixel and all the pixels with a value lower than 0.02 were removed. In this way, it was possible to improve the reconstruction of the shape and position of each grain (Figure 7 c-d). The images in Figure 7 c-d show the shape and position of the two grains already presented in Figure 4q and Figure 5a. In the case of the first grain from the top (Figure 7c), the longitudinal axis

was lying parallel to the plane of the picture showing the elongation of the crystal. The grain in Figure 7d was oriented perpendicular to the plane of the image, exposing a pseudo-hexagonal section of the crystal. When the reconstruction of all the 107 grains was completed, they were all summed in order to visualize the entire grain map of hemihydrate (Figure 7e).

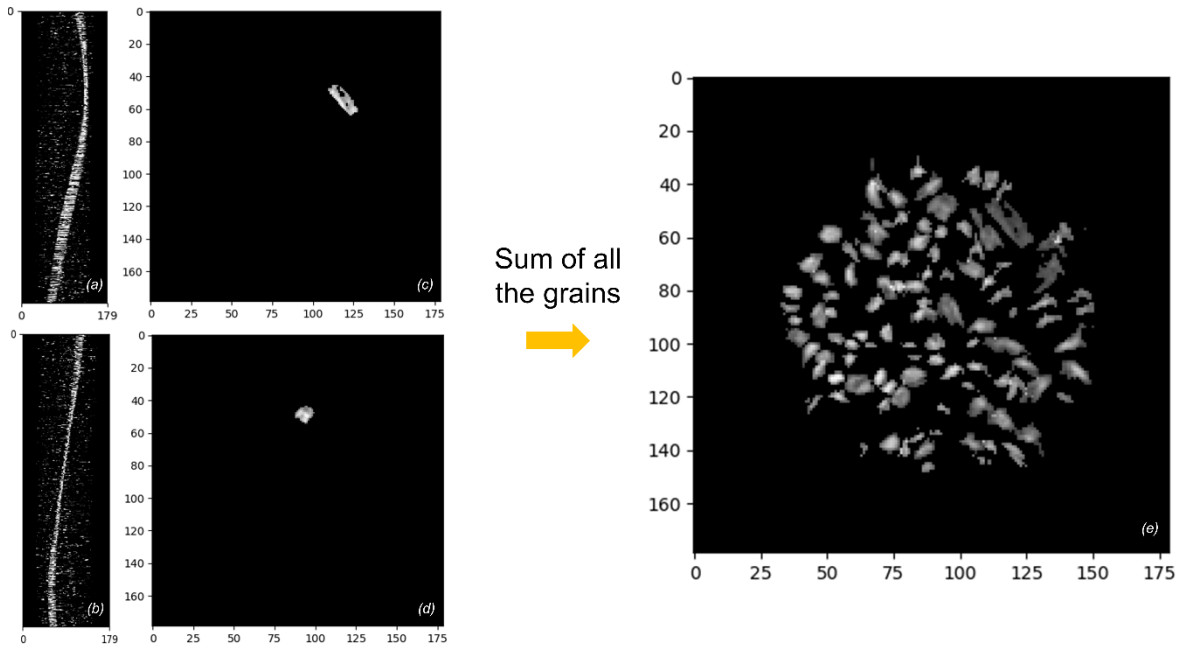

Figure 7 (a-b) Sinograms of two hemihydrate grains. (c-d) Reconstruction of the shape and position of the grains in the sample through iradon reconstruction of their sinograms. (e) Full grain map containing 107 indexed grain of dry hemihydrate.

From the indexing process of the gypsum dataset, 102 grains were indexed using the C 2/c lattice from (Boeyens & Ichharam, 2002). In this case, a higher intensity threshold, compared to the hemihydrate dataset, was used for the segmentation process. This permitted to index the largest gypsum grains. The grain map obtained from the indexing of gypsum grains is shown in Figure S5.

3.3.2. Orientation of the grains

The result of the indexing process is a matrix, called UBI, that is the inverse of the conventional (UB) (Busing & Levy, 1967). The UBI links the hkl indices (h) of the crystallographic planes of the individual crystals with their scattering vectors (g) with this equation (Eq.2):

$$h = UBI\ g \quad (2)$$

The crystal lattice vectors a,b,c in the sample co-ordinate system are given by the rows of the UBI matrix and plane normals can be derived via dot products for any of the indexed hemihydrate and gypsum grains. Orientations of both hemihydrate and gypsum grains are shown in Figure 8, where

three vectors show the crystallographic directions of the unit cells of hemihydrate grains (Figure 8a), and of gypsum (Figure 8b).

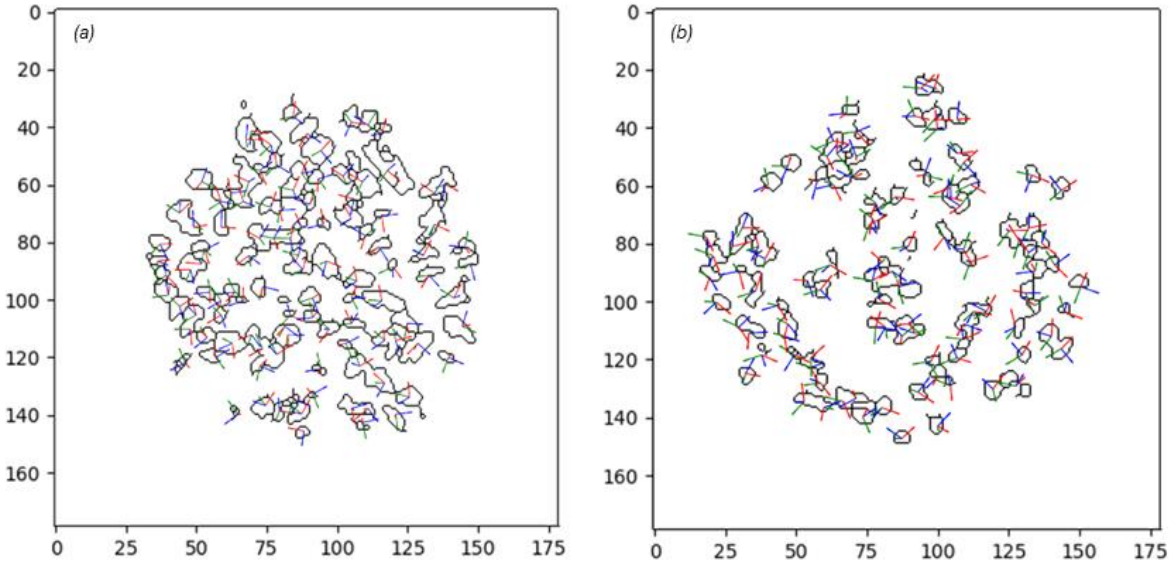

Figure 8 (a) Orientation of the three crystallographic axis of the hemihydrate grains, with *a* axis represented in green, *b* axis represented in blue and *c* axis represented in red. (b) Orientation of the three crystallographic axis of gypsum grains, with *a* axis represented in green, *b* axis represented in blue and *c* axis represented in red.

4. Discussion

4.1. Gaining access to textural information at the mesoscale

Previous works has highlighted the use of different X-ray tomography techniques to follow precipitation reactions in confined spaces (Godinho *et al.*, 2019) (Godinho *et al.*, 2016) (Anduix- Canto *et al.*, 2021). In comparison to these studies, the approach shown here presents a big advantage by introducing the crystallographic orientations of each indexed grain at the micron level. A direct correlation between the reconstructions made with s3DXRD (grain maps) and the reconstructions obtained from the PCT volumes can be established. Figure 9a and Figure 9c shows an example of the comparison between the indexed grains of dry α-hemihydrate reconstructed from the s3DXRD and the grains obtained from PCT respectively. All the grains shown in Figure 9a match with those present in Figure 9c. The majority of the smaller grains and fragments visible in the PCT reconstructions are not present in the s3DXRD grain map because the indexing process was tuned to select only the bigger grains. Once the grains have been characterized with both techniques, it is possible to merge the most useful information from both, namely the orientation of the crystallographic planes and the morphology and orientation in the space of the single grains. Figure

9b shows two selected grains, reconstructed from the s3DXRD diffraction data, with different orientations. The result of the combination is shown in Figure 9d where it is possible to identify in three dimensions the crystallographic orientations of the grains and to relate this to textural information from the 3D volume representation obtained from PCT. This allows to confirm that the direction of the elongation of the hemihydrate grains is parallel to the [001] direction (Follner *et al.*, 2002).

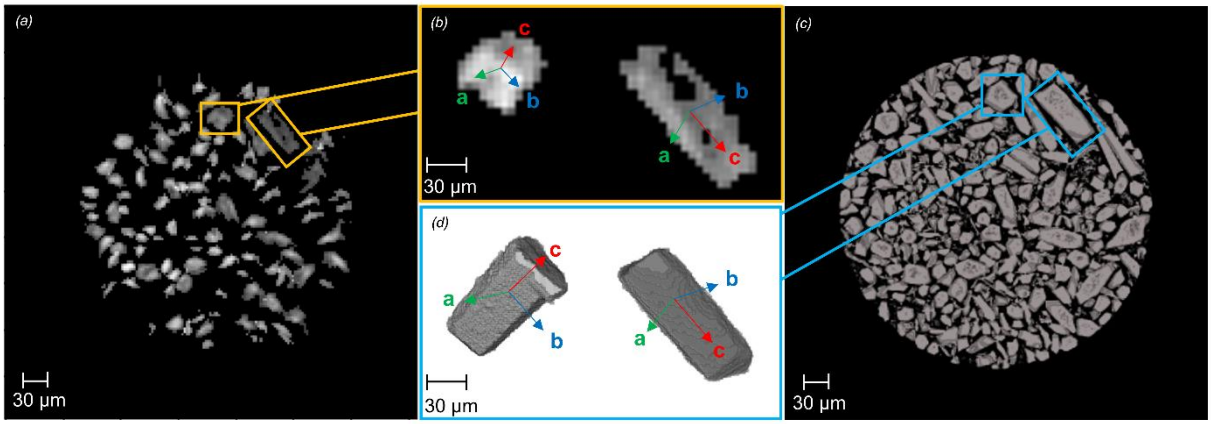

Figure 9 (a) Scanning 3DXRD grain map showing all the hemihydrate grains that were indexed. (b) Detail of the reconstruction of the two hemihydrate grains highlighted in (a) showing the orientation of the *a* (green), *b* (blue) and *c* (red) axis in the space. (c) 3D reconstruction of a stack of three PCT slices correspondent to the same portion of the sample shown in (a). (d) 3D reconstruction of the two hemihydrate grains also shown in (b), obtained from the segmentation of the single grains, showing the orientation of the *a* (green), *b* (blue) and *c* (red) axis in the space.

4.2. Dissolution of α-hemihydrate

We can make use of our approach to gain structural and crystallographic insights of the changes observed in hemihydrate grains during the hydration process. If we look at Figure 5 for example, it is possible to see how the morphology of the hemihydrate grains evolves during their dissolution, becoming thinner with time. Our combined approach allows establishing the crystallographic directions of preferential dissolution at the scale of a single grain. The two grains showed in Figure 9 are the same as those showed in Figure 5. The observed microscopic "lamination" of the grains, occurs through the directions perpendicular to the [001] crystallographic direction. This observation matches with a recent study by Mishra *et al.*, 2021 (Mishra *et al.*, 2021), who introduced a force-field model of the $CaSO_4$-H_2O system and reported the cleavage and hydration properties of the different calcium sulfate phases. This study reports that the (010) and (100) planes in hemihydrate, both perpendicular to the [001] direction, are the ones with higher solid-water interfacial energies, and therefore the less stable faces in water. An examination of the atomic structure of hemihydrate allows also determining that the number of bonds to be broken for ion removal from the (010) and (100)

faces is minimum compared to the (001). This is in good agreement with the observed higher reactivity of those faces.

The volumetric analysis of the PCT reconstructions of the dissolving hemihydrate grains give a potential way of measuring the dissolution rate and to account for the evolution of the reactive surface area (Rufe & Hochella, 1999) (Brandt & Bosbach, 2001) of bulk crystals, providing at the same time a 3D rendering of the changes in the morphology of the crystals. In Figure 10 two plots are shown relative to the evolution of the volume (Figure 10a) and normalised surface area (Figure 10b) for one grain of α-hemihydrate and one grain of gypsum during the hydration process. The two particles were segmented manually, with the *Dragonfly* software, from the full volumes during the hydration in order to show some quantitative measurements coupled with the morphological evolution. The red particle on the left of Figure 10 is the hemihydrate grain and the blue particle on the right is the gypsum grain that were used to calculate the volume and surface area variation during dissolution and growth. Since the two particles were segmented by hand, a segmentation range was considered. The upper limit of the segmentation range corresponded to the values of volume and surface area calculated by dilating the segmented particles. The lower limit of the segmentation range corresponded to the values calculated by eroding the segmented particles. It has been established that the rate of dissolution of crystals change substantially based on the scale of the measurement. Rates of dissolution measured on bulk crystals of calcite for example, were found to be higher than those measured on specific surfaces probably due to the fact that the crystal edges give a strong contribution to the dissolution due to their dense concentration of defects (Dove & Platt, 1996) (Arvidson *et al.*, 2003) (Lasaga & Luttge, 2001). Macroscopic measurements provide therefore mean values and are insensitive to high degrees of heterogeneity in the dissolution rates (Peruffo *et al.*, 2013).

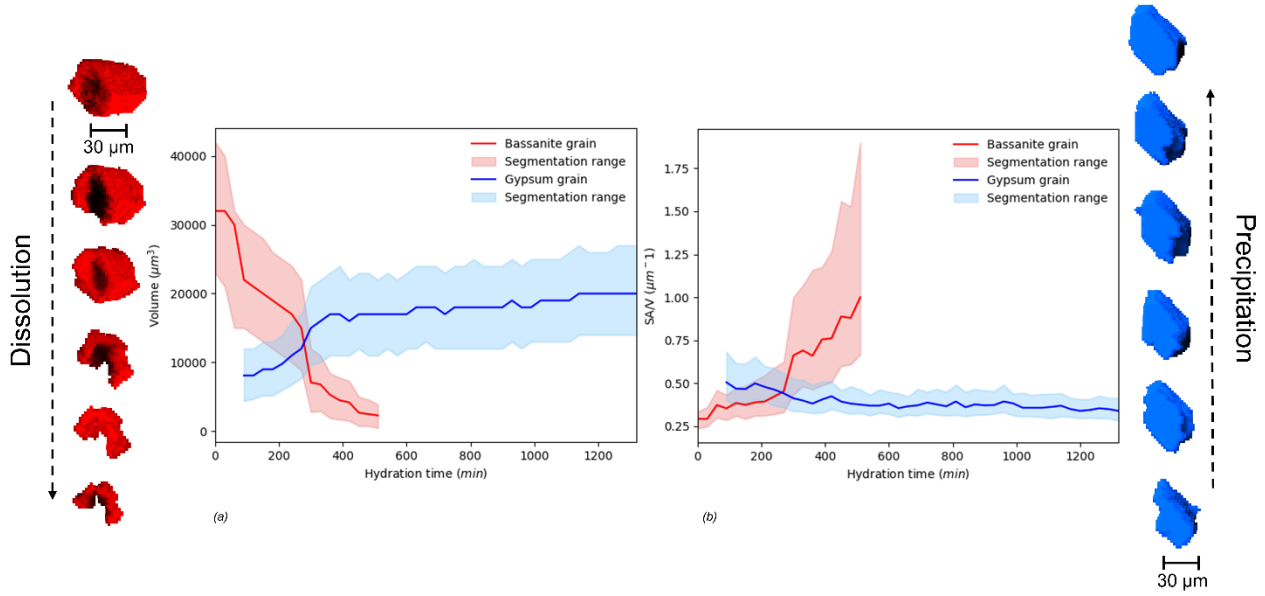

Figure 10 From the left: hemihydrate grain (in red) reconstructed from PCT segmentation showing the change in the morphology due to the dissolution. (a) Plot of the volume of the hemihydrate grain (red line), and gypsum grain (blue line). The range of segmentation is based on the values of volume and surface area obtained by dilating and eroding the segmented grain. (b) Plot of the surface area, normalized for the volume, of the hemihydrate grain (red line) and the gypsum grain (blue line). The segmentation range is obtained in the same way as for (a). Gypsum grain (in blue) reconstructed from PCT segmentation showing the growth of the crystal during the hydration process of the sample.

4.3. Precipitation of gypsum

The hydration process involves a phase transformation that can occur via (i) a complete dissolution of the starting material and a precipitation of the final material, (ii) a coupled dissolution-precipitation driven by local supersaturation built up at the reacting interfaces, or (iii) epitaxial relationships between the initial and final materials that could happen via templating or surface precipitation (Noiriel & Daval, 2017). The information about the grain orientations obtained in this work can be used to ascertain the precise mechanism of transformation of hemihydrate to gypsum. To this end, pole figures showing the orientations of the hemihydrate grains at the start of the experiment, and of gypsum grains at the end are shown in Figure 11. The results show that both hemihydrate and gypsum crystals are randomly oriented and no specific relative orientation is found between both. This indicates that epitaxial driven nucleation does not play a significant role in this system. Mechanisms (i) and (ii) are therefore possible. Given that the transport in the non-stirred capillary system used to contain the reactions is purely diffusive, it is likely that local gradients of concentration are present in the pore spaces between the grains, which could favour interfacial reactions such as those observed in other systems (Hellmann *et al.*, 2012) (Hellmann *et al.*, 2015).

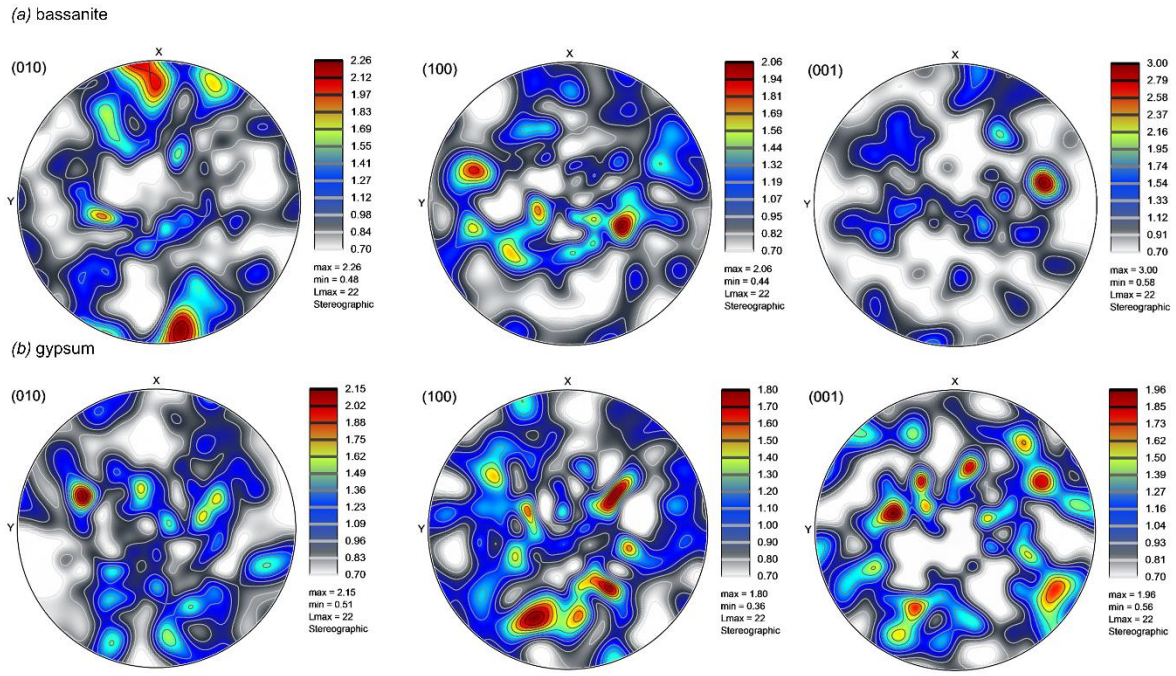

Figure 11 (a) Pole figures showing the distribution of the orientations of the starting hemihydrate grains for the directions [100], [010], and [001]. (b) Pole figures showing the distribution of the orientations of the final gypsum grains for the directions [100], [010], and [001]. All the figures were done using the software ATEX (Beausir & Fundenberger 2017).

Since no crystallographic relationships, that could demonstrate epitaxial growth, have been found between the dissolving hemihydrate crystals and the growing gypsum crystals, we can state that the setting of gypsum plaster is a two-step process, as already seen by Adrien et al. 2016 (Adrien *et al.*, 2016), involving the dissolution of hemihydrate and precipitation of gypsum. An example of this process is shown in Figure 12. The hemihydrate and gypsum particles shown in Figure 12 were extracted from the portion of the sample that was probed with both PCT and s3DXRD. The two particles were spatially close to each other, most likely as the result of the dissolution of hemihydrate and a local enrichment of the nearby pore solution that becomes supersaturated with respect to gypsum. Figure 12 reports the dynamic of the dissolution-precipitation process relative to the two segmented particles of hemihydrate and gypsum. The reconstructions follow the evolution in time from the presence of dry hemihydrate to the formation of gypsum and the complete dissolution of hemihydrate. The hemihydrate grain starts to dissolve from the center of the crystal, creating a pit that grows through the crystal along the [001] direction. The dissolution proceeds by dissolution of the pit walls (perpendicular to the [001] direction, highly reactive (100) and (010) planes). In the last part of the dissolution the grain shrinks adopting a ring shape. In our study, the nucleation of gypsum could not be observed due to the resolution limit, but growth of gypsum particles > 5 μm could be monitored. Depending on the formation conditions calcium sulfate minerals can adopt a wide variety

of crystal habits/morphologies, and textures (Van Driessche *et al.*, 2019). The morphology of the crystal that is formed in this case is platy, dominated by the {010} face.

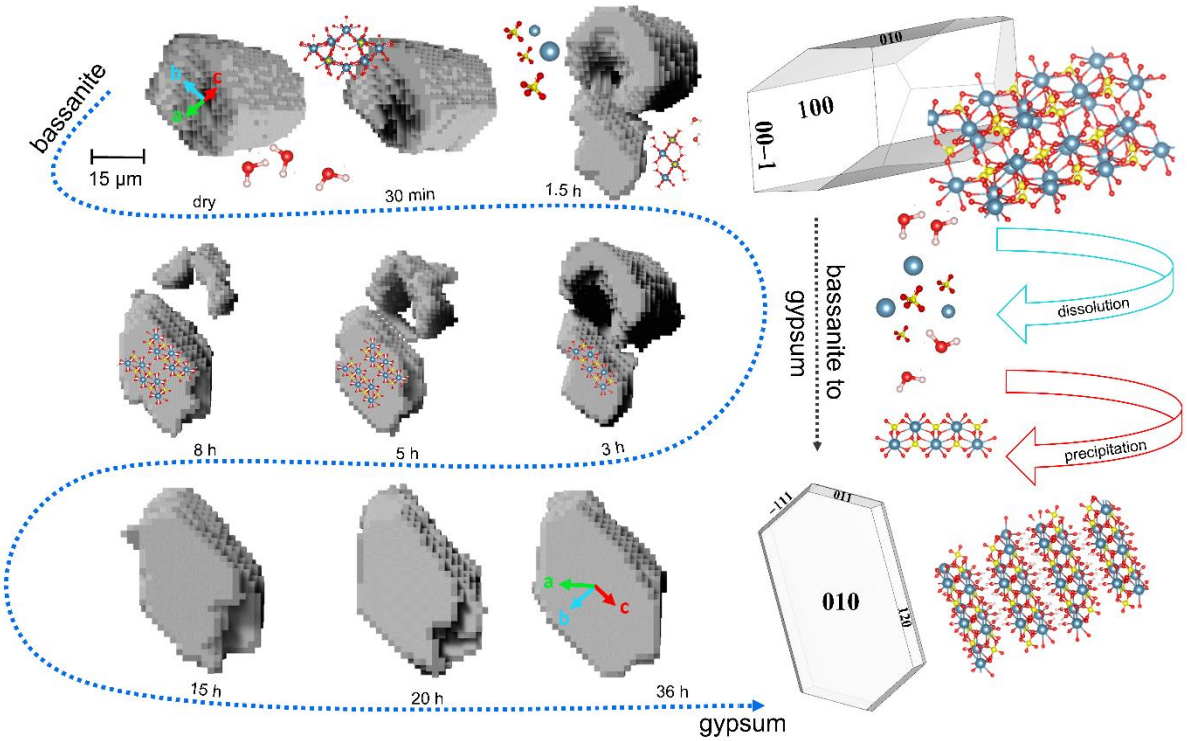

Figure 12 PCT reconstruction of segmented grains of hemihydrate and gypsum during the dissolution-precipitation process. The reconstructions are reported following the time evolution (indicated by the blue dashed arrow), from the dry conditions (presence of hemihydrate only) to the end of the hydration (presence of gypsum only). The PCT reconstructions are coupled with the crystallographic orientations calculated for the two specific grains from the s3DXRD analysis. On the right is reported a schematic representation of the transformation from the hemihydrate structure to the gypsum structure. Legend: grey balls = Ca atoms; yellow balls = S atoms; red balls = O atoms; white balls = water molecules.

5. Conclusions

The combination of the s3DXRD and PCT techniques revealed to be a powerful tool to study reaction kinetics in heterogeneous materials, such as the hydration of α-hemihydrate to gypsum, allowing a multi-scale characterization of the system and providing a link between crystallographic and textural information. This approach allowed us to exclude an epitaxial nucleation of gypsum crystals on the hemihydrate in our system, providing a 3D reconstruction of the dissolution-precipitation process *in-situ*. The volumetric information from the PCT data and the orientation of the grains from the s3DXRD data enabled the identification of the reacting faces of the crystals. We have shown that the (100) and (010) faces of hemihydrate are preferentially dissolved, leading to the formation of a layered texture, most likely coming from the presence of structural defects in certain layers of the

material. Indeed, structural defects (dislocations, point defects) are usually the loci where dissolution starts, given that thermodynamic conditions are favourable (Yukio Saito, 1996) (Lasaga, 1998) (Luttge *et al.*, 2019) (Lasaga & Luttge, 2001). While a considerable number of works have been performed on monitoring the dissolution of gypsum and anhydrite on specific surfaces, on a local level (Mbogoro *et al.*, 2011)(Peruffo *et al.*, 2013)(Feng *et al.*, 2017)(Bosbach & Rammensee, 1994), there are no local *in-situ* investigations available about the dissolution of hemihydrate because of the speed of the process. In this work, we observed the dissolution of hemihydrate at the mesoscale providing a link between microscopic (e.g., atomic force microscopy, atom-probe tomography, interferometry) and macroscopic studies of mineral weathering, thanks to the combination of information at the micron and single grain scale. The results obtained in this study clearly show the suitability of this diffraction and tomography approach, paving the way for possible future investigations. The integration of the powder diffraction patterns from the s3DXRD for example, could reveal the presence of amorphous phases while a statistical volumetric analysis of the dissolving hemihydrate crystals could provide an estimation of the dissolution rate of the bulk sample.

Acknowledgements ISTerre is part of Labex OSUG@2020. Use of the Geochemistry-Mineralogy platform at ISTerre is acknowledged. The authors wish to aknowledge the ESRF for provision of beamtime (Experiment number MA4498). We are also thankful to Dr. Pierre-Olivier Autran for useful insight on tomographic reconstructions and Dr. Marta Majkut for discussions on grains orientation calculations. The authors wish also to thank Dr. Irina Snigireva and Dr. Nathaniel Findling for SEM characterization of the samples and Dr. Catherine Dejoie for complementary high-resolution powder diffraction data from the ID22 beamline of the ESRF.

References

Abramoff M. D., Magalhães Paulo J., & Ram Sunanda J. (2004). *Biophotonics Int.* **11**, 36–42.

Adrien, J., Meille, S., Tadier, S., Maire, E. & Sasaki, L. (2016). *Cem. Concr. Res.* **82**, 107–116.

Anduix- Canto, C., Levenstein, M. A., Kim, Y., Godinho, J. R. A., Kulak, A. N., Niño, C. G., Withers, P. J., Wright, J. P., Kapur, N., Christenson, H. K. & Meldrum, F. C. (2021). *Adv. Funct. Mater*. **31**, 2107312.

Artioli, G., Cerulli, T., Cruciani, G., Dalconi, M. C., Ferrari, G., Parisatto, M., Rack, A. & Tucoulou, R. (2010). *Anal. Bioanal. Chem.* **397**, 2131–2136.

Artioli, G., Valentini, L., Voltolini, M., Dalconi, M. C., Ferrari, G. & Russo, V. (2015). *Cryst. Growth Des.* **15**, 20–23.

Arvidson, R. S., Ertan, I. E., Amonette, J. E. & Luttge, A. (2003). *Geochim. Cosmochim. Acta*. **67**, 1623–1634.

Ashiotis, G., Deschildre, A., Nawaz, Z., Wright, J. P., Karkoulis, D., Picca, F. E., Kieffer, J. (2015) *J. Appl. Crystallogr.* **48,** 510-519.

Ballirano, P., Maras, A., Meloni, S. & Caminiti, R. (2001). *Eur. J. Mineral.* **13**, 985–993.

Beausir B. & Fundenberger J. J. (2017).

Bensted, J. & Varma, S. P. (1971). *Nat. Phys. Sci.* **232**, 174–175.

Boeyens, J. C. A. & Ichharam, V. V. H. (2002). *Z. Für Krist.-New Cryst. Struct.* **217**, 9–10.

Bosbach, D. & Rammensee, W. (1994). *Geochim. Cosmochim. Acta*. **58**, 843–849.

Brandt, F. & Bosbach, D. (2001). *J. Cryst. Growth*. **233**, 837–845.

de Brito, J. & Flores-Colen, I. (2015). *Materials for Construction and Civil Engineering: Science, Processing, and Design*, Vol. edited by M.C. Gonçalves & F. Margarido, pp. 123–184. Cham: Springer International Publishing.

Busing, W. R. & Levy, H. A. (1967). *Acta Crystallogr.* **22**, 457–464.

Carretero, M. I. & Pozo, M. (2009). *Appl. Clay Sci.* **46**, 73–80.

Claret, F., Grangeon, S., Loschetter, A., Tournassat, C., De Nolf, W., Harker, N., Boulahya, F., Gaboreau, S., Linard, Y., Bourbon, X., Fernandez-Martinez, A. & Wright, J. (2018). *IUCrJ*. **5**, 150–157.

Coelho, A. A. (2018). *J. Appl. Crystallogr.* **51**, 210–218.

Dejoie, C., Coduri, M., Petitdemange, S., Giacobbe, C., Covacci, E., Grimaldi, O., Autran, P.-O., Mogodi, M. W., Šišak Jung, D. & Fitch, A. N. (2018). *J. Appl. Crystallogr.* **51**, 1721–1733.

Dove, P. M. & Platt, F. M. (1996). *Chem. Geol.* **127**, 331–338.

Feng, P., Brand, A. S., Chen, L. & Bullard, J. W. (2017). *Chem. Geol.* **460**, 25–36.

Follner, S., Wolter, A., Preusser, A., Indris, S., Silber, C. & Follner, H. (2002). *Cryst. Res. Technol. J. Exp. Ind. Crystallogr.* **37**, 1075–1087.

Freyer, D. & Voigt, W. (2003). *Monatshefte Für Chem. Chem. Mon.* **134**, 693–719.

Godinho, J. R. A., Gerke, K. M., Stack, A. G. & Lee, P. D. (2016). *Sci. Rep.* **6**, 33086.

Godinho, Ma, Chai, Storm, & Burnett (2019). *Minerals*. **9**, 480.

Hayashi, Y., Hirose, Y. & Seno, Y. (2015). *J. Appl. Crystallogr.* **48**, 1094–1101.

Hayashi, Y., Hirose, Y. & Setoyama, D. (2014). *Mater. Sci. Forum*. **777**, 118–123.

Hayashi, Y., Setoyama, D., Hirose, Y., Yoshida, T. & Kimura, H. (2019). *Science*. **366**, 1492–1496.

Hektor, J., Hall, S., Henningsson, N., Engqvist, J., Ristinmaa, M., Lenrick, F. & Wright, J. (2019). *Materials*. **12**, 446.

Hellmann, R., Cotte, S., Cadel, E., Malladi, S., Karlsson, L. S., Lozano-Perez, S., Cabié, M. & Seyeux, A. (2015). *Nat. Mater.* **14**, 307–311.

Hellmann, R., Wirth, R., Daval, D., Barnes, J.-P., Penisson, J.-M., Tisserand, D., Epicier, T., Florin, B. & Hervig, R. L. (2012). *Chem. Geol.* **294–295**, 203–216.

Henningsson, N. A., Hall, S. A., Wright, J. P. & Hektor, J. (2020). *J. Appl. Crystallogr.* **53**, 314–325.

Lasaga, A. C. (1998). Kinetic Theory in the Earth Sciences Princeton University Press.

Lasaga, A. C. & Luttge, A. (2001). *Science.* **291**, 2400–2404.

Lewry, A. J. & Williamson, J. (1994). *J. Mater. Sci.* **29**, 5524–5528.

Luttge, A., Arvidson, R. S., Fischer, C. & Kurganskaya, I. (2019). *Chem. Geol.* **504**, 216–235.

Mbogoro, M. M., Snowden, M. E., Edwards, M. A., Peruffo, M. & Unwin, P. R. (2011). *J. Phys. Chem. C.* **115**, 10147–10154.

Mishra, R. K., Kanhaiya, K., Winetrout, J. J., Flatt, R. J. & Heinz, H. (2021). *Cem. Concr. Res.* **139**, 106262.

Noiriel, C. & Daval, D. (2017). *Acc. Chem. Res.* **50**, 759–768.

Ossorio, M., Van Driessche, A. E. S., Pérez, P. & García-Ruiz, J. M. (2014). *Chem. Geol.* **386**, 16–21.

Paganin, D., Gureyev, T. E., Pavlov, K. M., Lewis, R. A. & Kitchen, M. (2004). *Opt. Commun.* **234**, 87–105.

Pedreño-Rojas, M. A., Flores-Colen, I., De Brito, J. & Rodríguez-Liñán, C. (2019). *J. Clean. Prod.* **215**, 444–457.

Peruffo, M., Mbogoro, M. M., Edwards, M. A. & Unwin, P. R. (2013). *Phys Chem Chem Phys*. **15**, 1956–1965.

Pons-Jiménez, M., Hernández-Altamirano, R., Cisneros-Dévora, R., Buenrostro-González, E., Oviedo-Roa, R., Martínez-Magadán, J.-M. & Zamudio-Rivera, L. S. (2015). *Fuel.* **149**, 66–77.

Poulsen, H. F. (2004). 3DXRD-a new probe for materials science Risø National Laboratory.

Rufe, E. & Hochella, M. F. (1999). *Science.* **285**, 874–876.

Saha, A., Lee, J., Pancera, S. M., Bräeu, M. F., Kempter, A., Tripathi, A. & Bose, A. (2012). *Langmuir*. **28**, 11182–11187.

Seiller, J., Bonnal, T., Adrien, J., Meille, S., Tadier, S., Maire, E. & Bonnin, A. (2021). *Constr. Build. Mater*. **304**, 124632.

Shepp, L. A. & Logan, B. F. (1974). *IEEE Trans. Nucl. Sci.* **21**, 21–43.

Singh, N. B. & Middendorf, B. (2007). *Prog. Cryst. Growth Charact. Mater.* **53**, 57–77.

Sørensen, H. O., Schmidt, S., Wright, J. P., Vaughan, G. B., Techert, S., Garman, E. F., Oddershede, J., Davaasambuu, J., Paithankar, K. S. & Gundlach, C. (2012).

Stawski, T. M., Van Driessche, A. E., Ossorio, M., Rodriguez-Blanco, J. D., Besselink, R. & Benning, L. G. (2016). *Nat. Commun.* **7**, 1–9.

Stawski, T. M., Van Driessche, A. E. S., Besselink, R., Byrne, E. H., Raiteri, P., Gale, J. D. & Benning, L. G. (2019). *J. Phys. Chem. C.* **123**, 23151–23158.

Taylor Harry FW (1997). Cement chemistry London.

Thomas, M. V. & Puleo, D. A. (2009). *J. Biomed. Mater. Res. B Appl. Biomater.* **88B**, 597–610.

Van Driessche, A. E., Kellermeier, M., Benning, L. G. & Gebauer, D. (2016). New perspectives on mineral nucleation and growth: from solution precursors to solid materials Springer.

Van Driessche, A. E. S., Benning, L. G., Rodriguez-Blanco, J. D., Ossorio, M., Bots, P. & García-Ruiz, J. M. (2012). *Science*. **336**, 69–72.

Wang, Y.-W., Kim, Y.-Y., Christenson, H. K. & Meldrum, F. C. (2012). *Chem. Commun.* **48**, 504–506.

Wright, J. (2005). *ImageD11*, https://github.com/FABLE-3DXRD/ImageD11/.

Yukio Saito (1996). Statistical Physics of Crystal Growth World Scientific.

Supporting information

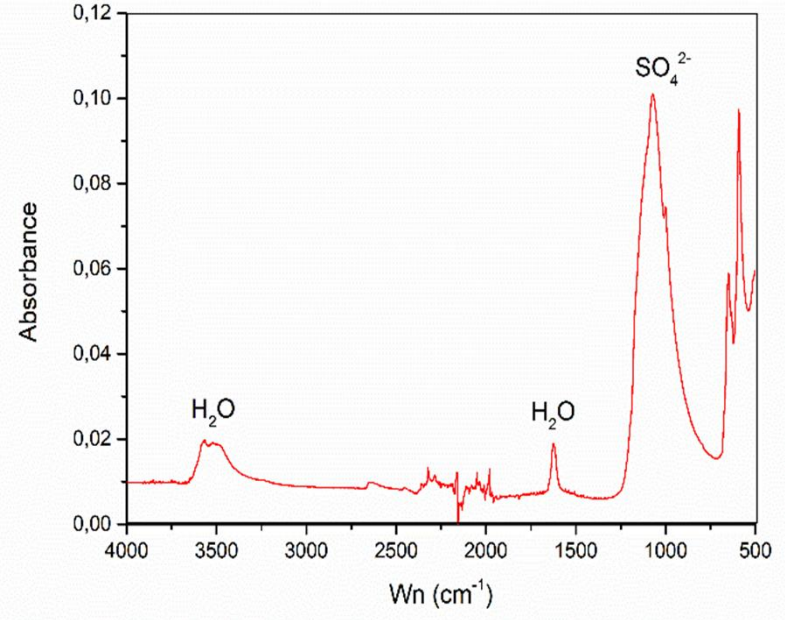

Figure S1 FTIR spectrum of the α-hemihydrate synthesized in this study.

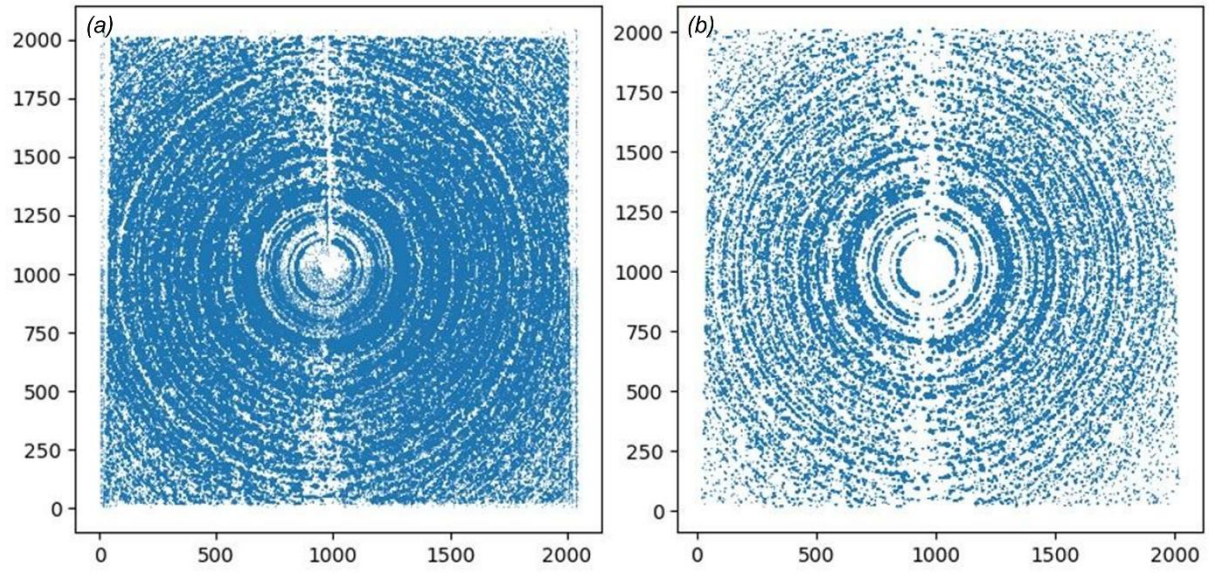

Figure S2 Peaks extracted from the segmentation process of *ImageD11* software: comparison between (a) low threshold value, (b) high threshold value.

Powder diffraction results

A Le Bail fit for the data collected at ID22 in the region 1.5-15° 2θ is shown in Figure S3a. Two different fits have been performed, one using the monoclinic space group I2 (Ballirano *et al.*, 2001)

(Figure S3b) and another with the trigonal space group $P3_121$ described in Abriel & Nesper, 1993 (Abriel & Nesper, 1993) (Fig. S3c). The first one yielded the best fit and has been chosen as best model to describe our system. It is possible to see in the 2θ region 3.2-3.55° (Figure S3c) that the trigonal model fits the peak using only the reflection with Miller index {020}, while the monoclinic model is able to fit the three existing peaks (with Miller indexes {101}{-101}{200}). Figure S4 shows Le Bail refinements in the 2θ region 1.8-18° collected at ID11 prior to start the hydration and at the end of the process. These were carried out to confirm the purity of the starting materials (Figure S4a) and the completeness of the hydration process (Figure S4b). Figure S4a confirms that the hemihydrate used for this experiment is the monoclinic I2 α-hemihydrate. Figure S4b reveals that a small amount of hemihydrate was still present at the end of the hydration process. This amount is very small indicating that the reaction is largely complete.

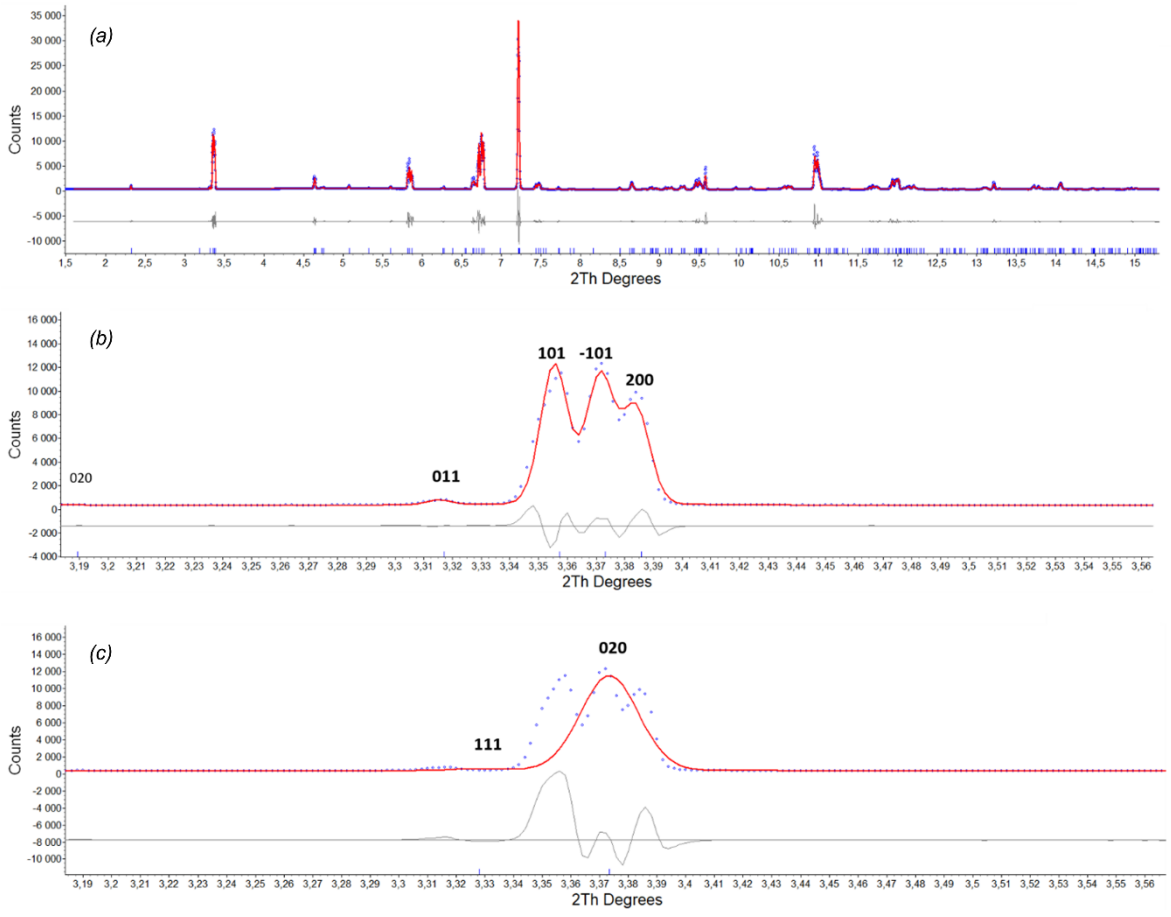

Figure S3 (a) Le Bail fit of the high resolution powder diffraction pattern collected at ID22 for the hemihydrate in the region 1.5-15° 2θ (experimental, blue dots, calculated, red continuous line). (b) Detail of the region 3.2-3.55 ° 2θ using the monoclinic I2 cell described in (Ballirano *et al.* 2001). (c) Detail of the region 3.2-3.55° 2θ using the trigonal $P3_121$ cell described in (Abriel & Nesper 1993).

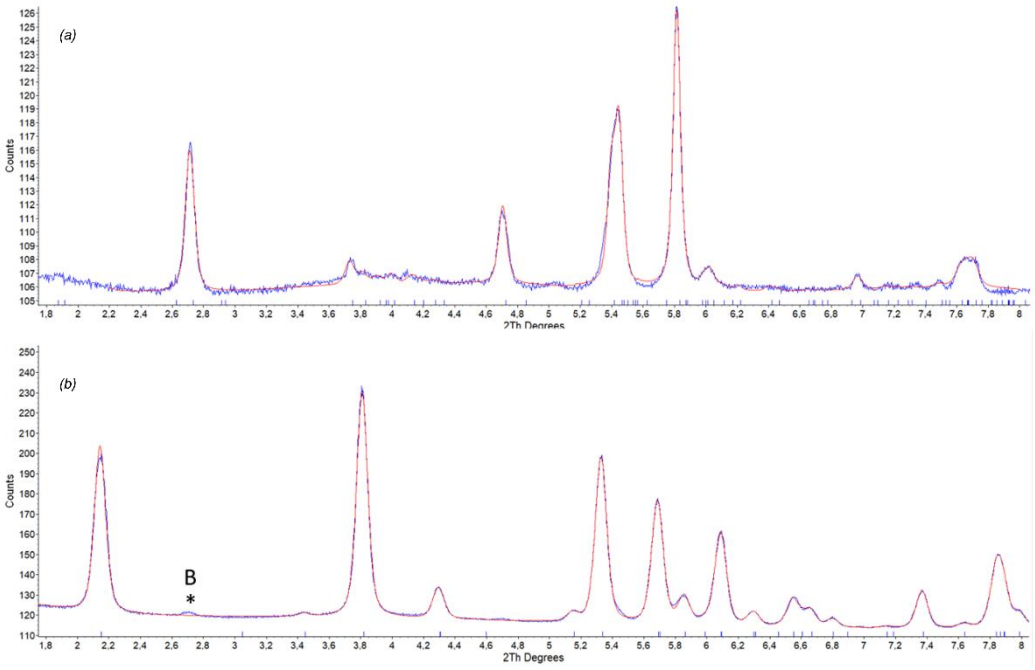

Figure S4 (a) Le Bail refinement of the powder diffraction pattern of the starting hemihydrate. The lattice parameters used are relative to the I2 structure (Ballirano *et al.* 2001). (b) Le Bail refinement of the gypsum (Boeyens & Ichharam 2002) obtained at the end of the hydration process. The remaining content of hemihydrate is negligible for the purpose of this study.

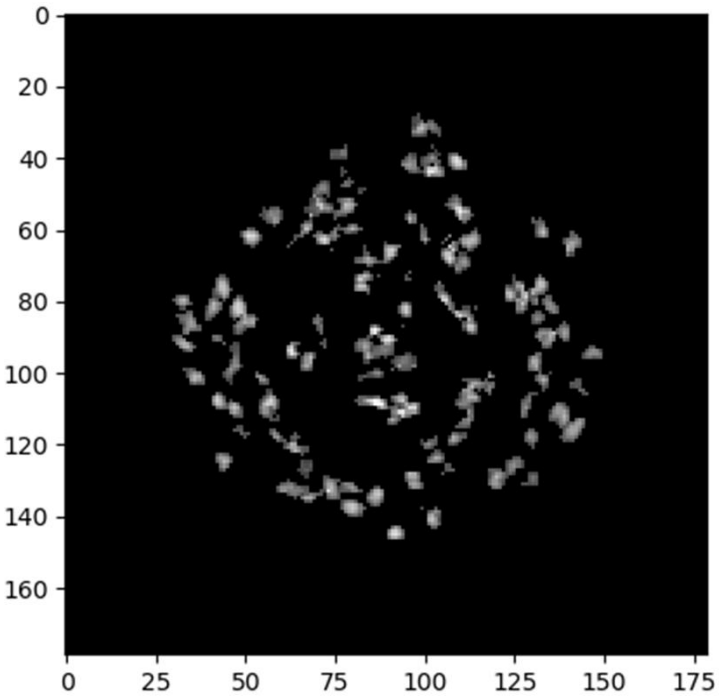

Figure S5 Grain map obtained from the indexing of 102 grains of gypsum.

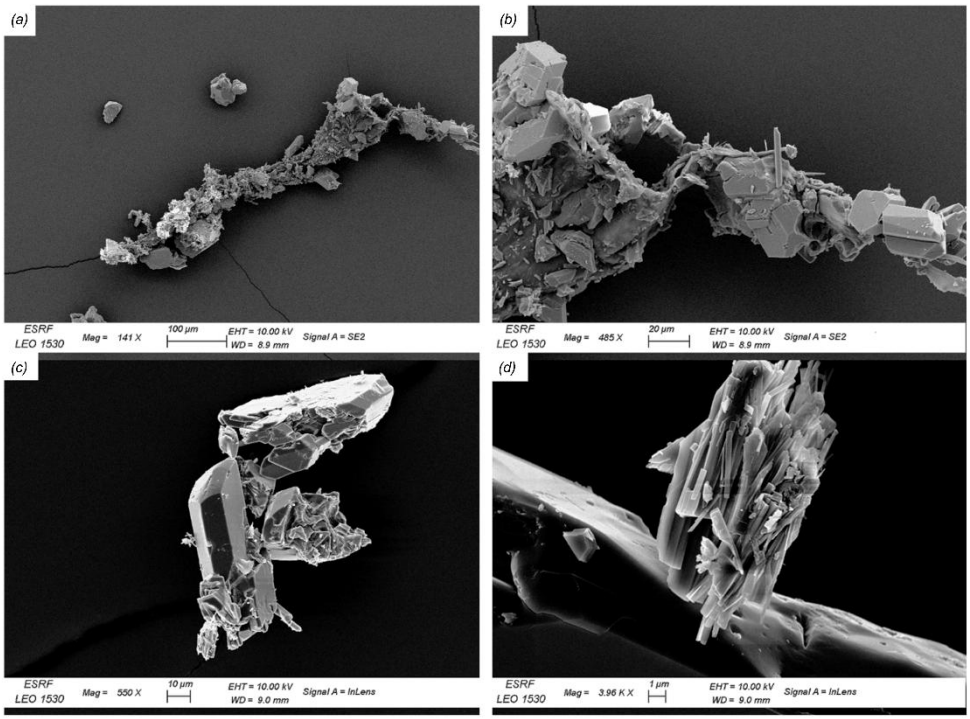

Figure S6 SEM images of the gypsum plaster formed after the hydration of hemihydrate that was monitored *in-situ*. (a) Portion of the gypsum crystals network extruded from the capillary. (b) Zoom on part of the sample showing different types of gypsum grains. (c) Detail of a tabular pseudo-rhombohedral gypsum crystal. (d) Detail of an agglomerate of gypsum needle shaped crystals.

References

Abriel, W. & Nesper, R. (1993). *Z. Krist.* **205**, 99–113.

Ballirano, P., Maras, A., Meloni, S. & Caminiti, R. (2001). *Eur. J. Mineral.* **13**, 985–993.

Boeyens, J. C. A. & Ichharam, V. V. H. (2002). *Z. Für Krist.-New Cryst. Struct.* **217**, 9–10.